

Consequences of high effective Prandtl number on solar differential rotation and convective velocity

Bidya Binay Karak^{1,2,*}, Mark Miesch^{2,†} and Yuto Bekki^{3‡}

¹*Indian Institute of Astrophysics, Koramangala, Bangalore 560034, India*

²*High Altitude Observatory, National Center for Atmospheric Research,
3080 Center Green Dr., Boulder, CO 80301, USA*

*Department of Earth and Planetary Science, The University of Tokyo,
7-3-1 Hongo, Bunkyo-ku, Tokyo 113-0033, Japan*

(Dated: November 6, 2018)

Observations suggest that the large-scale convective velocities obtained by solar convection simulations might be over-estimated (convective conundrum). One plausible solution to this could be the small-scale dynamo which cannot be fully resolved by global simulations. The small-scale Lorentz force suppresses the convective motions and also the turbulent mixing of entropy between upflows and downflows, leading to a large effective Prandtl number (Pr). We explore this idea in three-dimensional global rotating convection simulations at different thermal conductivity (κ), i.e., at different Pr. In agreement with previous non-rotating simulations, the convective velocity is reduced with the increase of Pr as long as the thermal conductive flux is negligible. A subadiabatic layer is formed near the base of the convection zone due to continuous deposition of low entropy plumes in low- κ simulations. The most interesting result of our low- κ simulations is that the convective motions are accompanied by a change in the convection structure that is increasingly influenced by small-scale plumes. These plumes tend to transport angular momentum radially inward and thus establish an anti-solar differential rotation, in striking contrast to the solar rotation profile. If such low diffusive plumes, driven by the radiative-surface cooling, are present in the Sun, then our results cast doubt on the idea that a high effective Pr may be a viable solution to the solar convective conundrum. Our study also emphasizes that any resolution of the conundrum that relies on the downward plumes must take into account angular momentum transport as well as heat transport.

INTRODUCTION

The outer layer of cool stars like the Sun is known to be convectively unstable whereby the energy from the interior to the surface is transported through convection. This, along with the global rotation of the star, drives differential rotation, meridional circulation, and the dynamo action responsible for generating magnetic activity [1, 2].

Although we have a tremendous success in modeling solar convection at granular scales through local Cartesian simulations [3], we face unavoidable challenges in simulating the global convection encompassing the full convection zone (CZ). It has been realized that simulations produce substantially higher convective velocities at large scales (small horizontal wave numbers) than that inferred from photospheric and helioseismic observations [4–6]. In fact, numerical models, which reproduce the solar surface granulations remarkably well, when extended to a larger extent, tend to produce larger power at low spectral wavenumber in comparison to photospheric observations [5]. This discrepancy between the observations and models is commonly known as the convective conundrum; see Section 1 of O’Mara *et al.* [7] for a detailed discussion.

A possible solution to the convective conundrum could be that the solar convection is driven by a non-local process. As argued by Spruit [8], the convection is driven by the efficient cooling at the surface. The low entropy

plumes generated near the surface penetrate the deeper CZ, in a process known as *entropy rain* [9, 10]. The non-local heat transport of these downward plumes maintains a subadiabatic layer where the enthalpy flux is still positive [9]. The existence of such a subadiabatic layer has been confirmed in a local Cartesian simulations with a smoothly varying heat conduction at the lower CZ based on either a Kramers-like opacity which is a function of temperature and density or a static profile of a similar shape [11]; also see Käpylä *et al.* [12] for the extension of this study in the spherical geometry with dynamo.

Another possible solution of the convective conundrum, as proposed by Hotta *et al.* [13], could be the suppression of the convective velocity due to the Lorentz force of the dynamo-generated magnetic field. In many global MHD simulations, it has been seen that the magnetic field reduces the convective velocity through the suppression of shear and thus effectively increasing the turbulent viscosity (ν_{eff}) [14–16]. The effect of this has been realized in the transition to the solar-like differential rotation from the anti-solar profile [14, 15]. Solar-like differential rotation is characterized by faster equator and slower poles (equatorward $\nabla\Omega$). The opposite scenario where the equator rotates slower than the poles (poleward $\nabla\Omega$), is referred to as the anti-solar (AS) differential rotation. In simulations cited above, the magnetic field is produced only from the large-scale dynamo. However, the small-scale dynamo also produces an immense amount of magnetic flux in the whole CZ and thus the

effect could be profound [16–19]. Recently, Hotta et al. [13, 20] carried out a set of global convection simulations with and without rotation and found about 50% reduction in convective velocities due to the small-scale magnetic field in their highest resolution simulation that they could achieve. Another effect of magnetism is that it reduces the turbulent mixing of entropy fluctuations in downflow plumes. This decreases the effective thermal diffusivity (κ_{eff}). Therefore, the magnetism effectively increases the turbulent Prandtl number $\text{Pr}_{\text{eff}} (= \nu_{\text{eff}}/\kappa_{\text{eff}})$ if the convection is essentially magnetized.

Since any global simulations at present cannot fully capture the small-scale dynamo action as realized in the real Sun, the effects are often modeled as an enhanced effective Prandtl number Pr_{eff} to investigate the properties of the magnetized stellar convection. At this end, O’Mara et al. [7] carried out a set of convection simulations at varying Pr and they showed that the convective velocity decreases with the increase of Pr_{eff} . In local Cartesian simulations, Bekki et al. [21] also find a similar result of decreasing convection velocity with the increase of Pr. They further demonstrated that a subadiabatic layer near the base of the CZ is formed by continuous deposition of low-entropy downward plumes. The depth of this layer increases with the decrease of horizontal thermal diffusivity.

If solar convection is largely driven by entropy rain, caused by the radiative surface cooling and/or by the large effective Pr caused by the magnetic field, then this is certainly an encouraging thought because both of these effects act to reduce the convective velocity. We may hope that in a realistic scenario these effects might solve the solar convective conundrum. However, the problem is more subtle. These downward plumes can also transport angular momentum inward and thus produce a radially decreasing rotation rate i.e., an anti-solar differential rotation. As the simulations mentioned above [7, 10, 11, 13, 20, 21] were all performed in local geometry without rotation, this effect could not be explored.

In this study, we explore the effect of downward plumes in forming the subadiabatic layer and particularly in transporting angular momentum in rotating convection. We perform a few sets of rotating and non-rotating global convection simulations in spherical geometry at different Pr. We find that at larger Pr the convective velocity is suppressed and a subadiabatic layer is formed near the base of the CZ due to continuous deposition of low entropy plumes. However, our results are quantitatively different than the previous non-rotating (local) Cartesian simulations [7, 21]. The most interesting and unforeseen result of our simulations is that the inward transport of angular momentum by plumes leads to an anti-solar differential rotation in high-Pr regime, despite the stronger rotational influence as quantified by the lower Rossby number.

NUMERICAL MODEL

In our study we solve the hydrodynamic (non-magnetic) equations in rotating spherical geometry under the anelastic approximation using the pseudo-spectral code, Rayleigh; see Featherstone and Hindman [22] for details. With this approximation, thermodynamic variables are linearized about a spherically symmetric, time-independent reference state with density $\bar{\rho}$, pressure \bar{P} , temperature \bar{T} , and specific entropy \bar{S} and fluctuations about this state are represented by ρ , P , T , and S , respectively. The reference state is assumed to be in an adiabatically-stratified hydrostatic equilibrium; see Appendix C of Featherstone and Hindman [22] for more details.

With this approximation, the continuity equation reduces to

$$\nabla \cdot (\bar{\rho}\mathbf{v}) = 0, \quad (1)$$

where \mathbf{v} is the velocity field. The momentum equation is given by

$$\bar{\rho} \left[\frac{D\mathbf{v}}{Dt} + 2\boldsymbol{\Omega}_0 \times \mathbf{v} \right] = -\bar{\rho} \nabla \frac{P}{\bar{\rho}} - \frac{\bar{\rho}S}{c_p} \mathbf{g} - \nabla \cdot \mathcal{D}. \quad (2)$$

Here \mathbf{g} is the gravitational acceleration, c_p is the specific heat at constant pressure, $\boldsymbol{\Omega}_0 = (\cos\theta, -\sin\theta, 0)\Omega_0$ is the angular velocity vector, and the viscous stress tensor \mathcal{D} is given by

$$\mathcal{D}_{ij} = -2\bar{\rho}\nu \left[e_{ij} - \frac{1}{3}(\nabla \cdot \mathbf{v})\delta_{ij} \right], \quad (3)$$

where e_{ij} is the strain rate tensor, ν is the kinematic viscosity, and δ_{ij} is the Kronecker delta. The energy equation is given by

$$\bar{\rho}\bar{T} \frac{DS}{Dt} = \nabla \cdot [\kappa\bar{\rho}\bar{T}\nabla S] + 2\bar{\rho}\nu \left[e_{ij}e_{ij} - \frac{1}{3}(\nabla \cdot \mathbf{v})^2 \right] + Q_{\text{heat}} + Q_{\text{cool}}, \quad (4)$$

where the thermal diffusivity is denoted by κ , and Q_{heat} and Q_{cool} are the internal heating and cooling. Following previous studies [7, 22], we use a functional form of Q_{heat} that depends only on the background pressure profile such that

$$Q_{\text{heat}}(r) = \alpha [\bar{P}(r) - \bar{P}(r_o)]. \quad (5)$$

The normalization constant α is chosen so that

$$L_{\odot} = 4\pi \int_{r_i}^{r_o} r^2 Q_{\text{heat}}(r) dr, \quad (6)$$

where L_{\odot} is the stellar luminosity, r_i and r_o are the inner and outer radii of the computation domain. The radial

dependence of the net radiative heat flux (see, for example, Figure 6 of Featherstone and Hindman [22]) is then defined as

$$F_{\text{r}}(r) = \frac{L_{\odot}}{4\pi r^2} - \frac{1}{r^2} \int_{r_i}^r r'^2 Q_{\text{heat}}(r') dr'. \quad (7)$$

For Q_{cool} , we use the same form as given in Hotta *et al.* [23] and Bekki *et al.* [21] i.e.,

$$Q_{\text{cool}}(r) = -\frac{1}{r^2} \frac{\partial}{\partial r} (r^2 F_{\text{s}}), \quad (8)$$

where

$$F_{\text{s}} = \frac{L_{\odot}}{4\pi r^2} \exp \left[-\left(\frac{r - r_o}{H_{\text{p}}} \right)^2 \right], \quad (9)$$

with H_{p} being the pressure scale height.

Finally, the linearized equation of state is given by

$$\frac{\rho}{\bar{\rho}} = \frac{P}{\bar{P}} - \frac{T}{\bar{T}} = \frac{P}{\gamma \bar{P}} - \frac{S}{c_p}, \quad (10)$$

which is obtained by assuming the ideal gas law $\bar{P} = \mathcal{R} \bar{\rho} \bar{T}$, where γ is the adiabatic index of the gas and \mathcal{R} is the gas constant.

Our model is constructed using an adiabatic (constant \bar{S}), polytropic background state, which is specified with seven inputs, namely $r_i = 0.7R_{\odot}$, $r_o = R_{\odot} = 6.96 \times 10^{10}$ cm, the polytropic index $n_p = 1.5$, the number of density scale heights within the domain $N_{\rho} = 3$ (see the green curve in Figure 1a of Featherstone and Hindman [22]), the mass below the inner boundary $M_i = 1.989 \times 10^{33}$ gm, the density at the inner boundary $\rho_i = 0.1805$ g cm $^{-3}$, and $c_p = 3.5 \times 10^8$ erg g $^{-1}$ K $^{-1}$.

In our model at both boundaries, we impose impenetrable and stress-free conditions such that

$$v_r = \frac{\partial}{\partial r} \left(\frac{v_{\theta}}{r} \right) = \frac{\partial}{\partial r} \left(\frac{v_{\phi}}{r} \right) = 0 \Big|_{r=r_i, r_o}. \quad (11)$$

For entropy we have the following conditions:

$$\frac{\partial S}{\partial r} \Big|_{r=r_i} = 0, \quad S(r_o) = 0. \quad (12)$$

Thus there is no diffusive entropy flux across the bottom boundary. However, the convection is driven by depositing heat in the domain through Q_{heat} (Equation (5)) which decreases to zero at the outer boundary and by cooling the upper part through Q_{cool} (Equation (8)).

RESULTS

We perform three sets of simulations, namely, at the solar rotation rate (R1), five times solar rotation (R5) and without rotation (R0). In each set, we vary the Prandtl

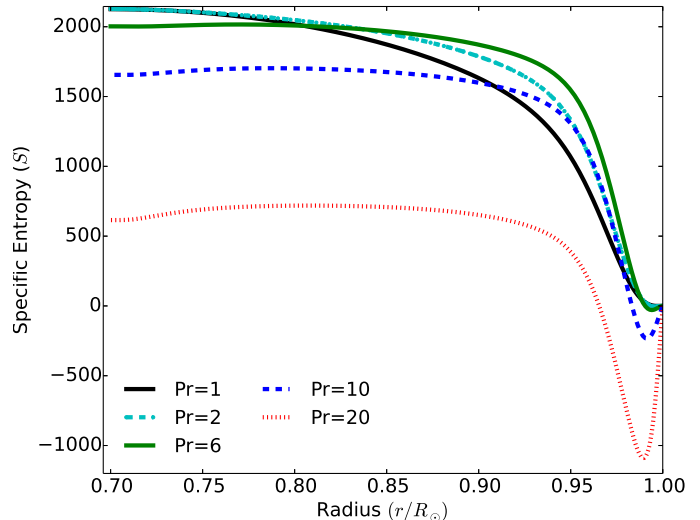


FIG. 1. Radial dependence of the specific entropy $\langle S \rangle_{\theta, \phi, t}$ in unit of erg g $^{-1}$ K $^{-1}$ obtained from Runs R1P1 (black), R1P2 (cyan), R1P6 (green), R1P10 (blue), and R1P20 (red).

number Pr from 1 to 20 by decreasing the thermal diffusivity κ alone. Each run is labeled with RxPy which represent a simulation at x times solar rotation rate and at $\text{Pr} = y$; see Table I. All simulations are run for several thermal diffusion times and we consider the results only after they have reached the thermally relaxed state. During this state, the flow remains statistically stationary.

Formation of Subadiabatic Layer

Figure 1 shows the specific entropy $\langle S \rangle_{\theta, \phi, t}$ averaged over time and the horizontal dimensions as a function of radius, from the R1 set of simulations (R1P1–R1P20). We observe that in most of the CZ, particularly for the larger Pr runs, the entropy stratification is close to adiabatic and at the surface it goes to zero due to the imposed boundary condition. The cooling layer near the surface tries to reduce the entropy just below the surface and this causes a narrow subadiabatic layer (with $dS/dr > 0$) there. This effect is more pronounced at smaller κ (larger Pr) because the thermal diffusion is insufficient to cause the local cooling to spread. The resulting buoyant acceleration then establishes the convection. Similar behavior is also seen in the previous local non-rotating simulations of Bekki *et al.* [21], although they do not have fixed entropy boundary condition at the top.

As Pr is increased, we start getting a positive mean entropy gradient in the lower part of the domain and thus a subadiabatic layer in which $dS/dr > 0$ is formed. In Figure 2, we show the subadiabaticity δ which is defined

TABLE I. Simulation summary. In all simulations, ν is fixed at $8 \times 10^{12} \text{ cm}^2 \text{ s}^{-1}$. Thus in each set of simulations, the Prandtl number $\text{Pr} = \nu/\kappa$ is varied by changing κ . The Taylor number, $\text{Ta} = (2\Omega_0 d^2/\nu)^2$ with $d = 0.3R_\odot$, in the R1 set of simulations is 8×10^4 , while in R5 set it is 2×10^6 . Other parameters are defined as follows: the Rayleigh number $\text{Ra} = \frac{GM_\odot d^3}{R_\odot^2 \nu \kappa C_p} \Delta S$, where $\Delta S = \langle S \rangle_{\theta, \phi}|_{\text{max}} - \langle S \rangle_{\theta, \phi}|_{\text{min}}$ (in unit of $\text{erg g}^{-1} \text{K}^{-1}$) is the entropy contrast across the layer. The rms value of the convective velocity $u_{\text{rms}} = \langle \sqrt{(v_r - \langle v_r \rangle_\phi)^2 + (v_\theta - \langle v_\theta \rangle_\phi)^2 + (v_\phi - \langle v_\phi \rangle_\phi)^2} \rangle_{\{r, \theta, \phi, t\}}$ in m s^{-1} , the convective Rossby number $\text{Ro}_c = \sqrt{\frac{\text{Ra}}{\text{PrTa}}}$, Rossby number $\text{Ro} = u_{\text{rms}}/(2\Omega_0 l_{\text{corr}})$ with $l_{\text{corr}} = d/2\pi$ is an estimate of the largest eddies, $\text{Pe} = u_{\text{rms}} l_{\text{corr}}/\kappa$, L_e^p is peak of the enthalpy flux, d_{sa} is the spherically-averaged width of the subadiabatic layer (with $\delta < 0$) in Mm, formed in the lower CZ in the statistically stationary state, f_d is the filling factor of the downflow, $\overline{\text{RS}}_r, \overline{\text{RS}}_\theta$ respectively show the strength of the radial and latitudinal Reynolds stresses averaged over the northern hemisphere in units of 10^{15} g s^{-2} , $\Delta_\Omega^{(r)} = \Omega(R_\odot, 90^\circ) - \Omega(0.71R_\odot, 90^\circ)$, and $\Delta_\Omega^{(\theta)} = 0.5[2\Omega(R_\odot, 90^\circ) - \Omega(R_\odot, 30^\circ) - \Omega(R_\odot, 120^\circ)]$.

Run	Pr	N_r, N_θ, N_ϕ	ΔS	$\text{Ra}[10^4]$	Ro_c	u_{rms} (m/s)	Ro	Pe	L_e^p	d_{sa} (Mm)	f_d	$\overline{\text{RS}}_r, \overline{\text{RS}}_\theta$	$\Delta_\Omega^{(r)}, \Delta_\Omega^{(\theta)}$
R1P1	1	128,192,384	2282	2.5	0.56	77.7	0.45	20.3	0.65	0.0	0.44	1.48, 6.8	14.8, 41.5
R1P2	2	128,256,512	2319	5.2	0.57	91.7	0.53	47.9	0.94	0.0	0.42	-1.91, 6.8	8.8, 21.9
R1P6	6	128,512,1024	2477	17	0.59	91.2	0.53	143	1.02	45.3	0.42	-6.03, 4.7	-15.8, -2.0
R1P10	10	128,1024,2048	2499	28	0.59	85.9	0.50	224	1.01	60.9	0.42	-6.41, 3.6	-20.7, -3.6
R1P20	20	200,2048,4096	2389	53	0.58	77.7	0.45	406	0.98	77.6	0.42	-6.25, 2.7	-24.4, -2.1
R5P1	1	128,192,384	4086	4.6	0.15	10.4	0.012	2.7	0.03	0.0	0.37	0.04, 0.1	1.2, 2.2
R5P2	2	128,192,384	6380	14	0.19	40.7	0.047	21.2	0.41	0.0	0.49	1.73, 2.3	19.9, 44.2
R5P6	6	128,512,1024	5271	35	0.17	59.9	0.069	93.8	0.88	0.0	0.47	2.25, 3.6	22.6, 57.3
R5P20	20	200,2048,4096	4412	99	0.16	54.2	0.062	283	0.92	20.4	0.46	-0.75, 1.4	7.3, 28.3
R0P1	1	128,192,384	1886	2.1	∞	140.8	∞	36.8	1.17	90.4	0.31
R0P2	2	128,192,384	2196	4.9	∞	130.6	∞	68.2	1.19	90.4	0.33
R0P6	6	128,512,1024	1972	13	∞	111.0	∞	174.1	1.02	92.9	0.35
R0P20	20	200,2048,4096	2100	48	∞	80.5	∞	420.0	1.00	95.4	0.35

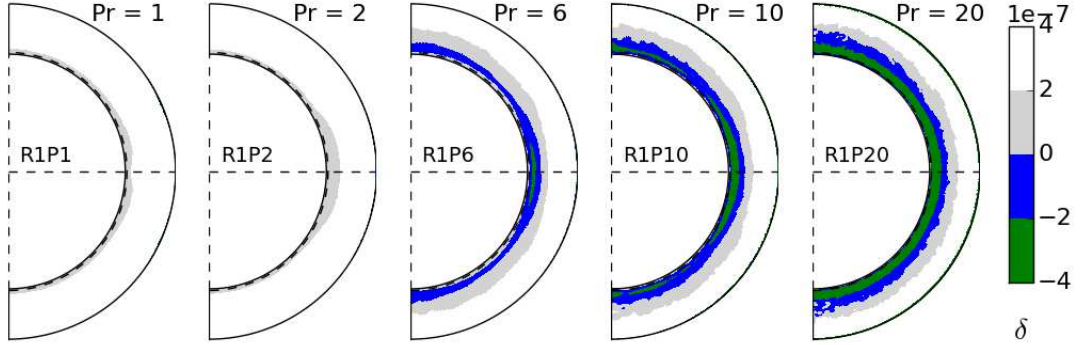


FIG. 2. Superadiabaticity $\delta = -(H_p/c_p) \frac{d}{dr} \langle S \rangle_{\theta, \phi, t}$ obtained by averaging over azimuth and time from Runs R1P1–R1P20. Note the blue and green colors show the subadiabatic layer ($\delta < 0$) developed in the statistically stationary convection.

as

$$\delta = \Delta - \Delta_{\text{ad}} = -\frac{H_p}{c_p} \frac{d}{dr} \langle S \rangle_{\theta, \phi, t}, \quad (13)$$

where $\Delta = d \ln T / d \ln P$ is the logarithmic temperature gradient and Δ_{ad} is the adiabatic one. This subadiabatic layer formed in our simulations is a consequence of the accumulation of low entropy plumes. As demonstrated by Bekki et al. [21] [also see 10, 11], when κ is small, the horizontal thermal diffusion of low entropy plumes is reduced and thus they can travel much deeper into the CZ before mixing with the surrounding fluid. This is clearly seen

in Figure 3 for the entropy perturbation. For $\text{Pr} = 10$, the plumes reach all the way to the bottom of the CZ without losing their thermal content and the convection in this case is plume-like, while in the case of $\text{Pr} = 1$, the plumes are wider and less prominent, appearing together with columnar downflow lanes (banana cells). Thus at larger Pr , the downflow plumes accumulate in the lower CZ, forming the subadiabatic stratification. In a statistically stationary state, the accumulation of low entropy plumes is compensated by vertical advection and diffusion.

Interestingly, the enthalpy flux (F_{enth}) is positive even

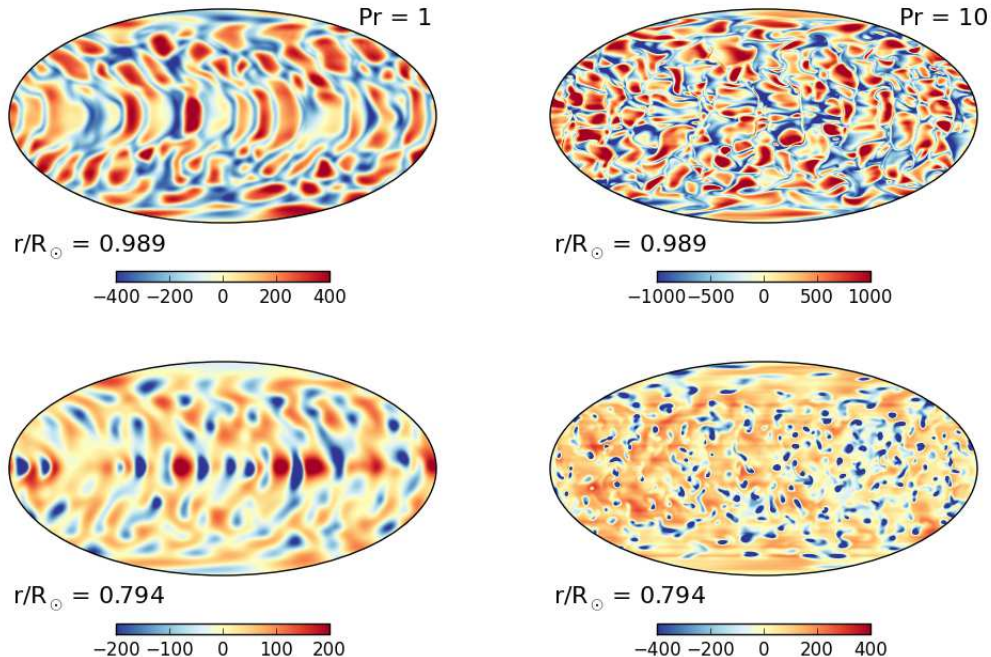


FIG. 3. Entropy fluctuation $S - \langle S \rangle_{\phi}$ in $\text{erg g}^{-1} \text{K}^{-1}$ at two different radial layers (top panels: near the upper boundary; bottom: near the base of the CZ) from Run R1P1 (left panels), and Run R1P10 (right panels).

near the base of the CZ where the subadiabatic layer is formed; see Figure 4. Thus in this subadiabatic layer the thermal energy is transported upward, which clearly manifests the nonlocal convective heat transport, possibly in a form of the non-gradient (*Deardorff*) flux as discussed in Brandenburg [9] and Käpylä et al. [11]. This layer is distinct from the overshoot region where the plumes are decelerated due to buoyancy and energy is transported downward.

We note that in non-rotating simulations, Bekki et al. [21] detected the subadiabatic layer even at $Pr = 1$ and 2, for which we have not found any such layer. Although their simulations are performed in local geometry and with a different surface boundary condition, we suspect rotation to be the major cause of producing distinct results. To explore this, we analyze the non-rotating simulations. We find that for all values of Pr , starting from 1, we get a subadiabatic layer; see Runs R0P1–R0P20 in Table I. Therefore, the rotation which is not included in previous simulations of Bekki et al. [21] is the cause of the difference between their results and ours. The Coriolis force inhibits the downward propagation of the plumes, suppressing the formation of the subadiabatic layer. Due to the same reason, the R5 series of simulations ($\Omega_0 = 5\Omega_{\odot}$) show a thin subadiabatic layer only at $Pr = 6$ and 20; see Figure 5.

Plumes at different latitudes feel a different effect of the Coriolis force. Near poles, plumes approach the sub-

adiabatic layer almost vertically, while in low latitudes they travel at an angle or are subsumed into banana cells. Hence, we expect the extent of the subadiabatic layer to decrease as we move away from the poles. Interestingly, in the R1 set of simulations, we do not find any significant latitudinal variation of the subadiabatic layer (Figure 2). However, in the R5 set of simulations, we do see some latitudinal variation, although not monotonic; see Figure 5. The reason is that the dominant structure of rapidly rotating convection transitions from banana cells at low latitudes to plumes at high latitudes. As in previous rotating global convection simulations at moderate Ra , convection is least efficient in the mid-latitude transition region [1, 24]. Here this lower efficiency is manifested as the absence of a subadiabatic layer at mid-latitudes.

A similar phenomenon has been seen previously in the local f-plane simulations of Brummell et al. [25] and the global convection simulations of Miesch et al. [26]. Both found that the convective overshoot region was wider near the equator and poles and thinner at mid-latitudes. However, their simulations included a radiative zone with a highly subadiabatic stratification and the overshoot region was characterized by a negative value of the convective enthalpy flux. By contrast, the subadiabatic stratification in our simulations is relatively weak and the enthalpy flux is everywhere positive (radially outward).

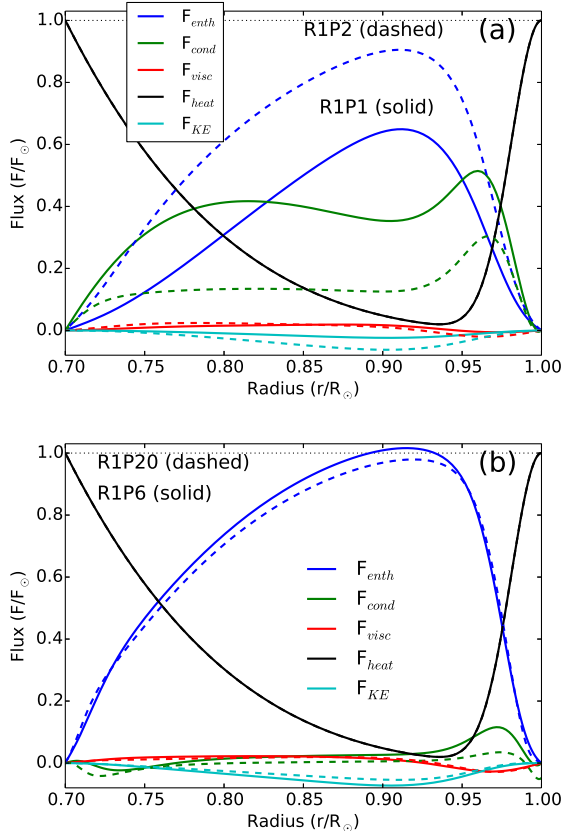


FIG. 4. Radial variations of enthalpy flux (blue), kinetic energy flux (cyan), conductive flux (green), viscous flux (red), and net heating and cooling flux $F_r + F_s$ (black) which includes the heating (decreasing monotonically to zero at the surface) and cooling (significant only near the surface). All fluxes are normalized by $F_\odot = L_\odot/4\pi r^2$. See Featherstone and Hindman [22] for the definitions of these fluxes. (a) Obtained from Runs R1P1 (solid) and R1P2 (dashed). (b) From Runs R1P6 (solid) and R1P20 (dashed).

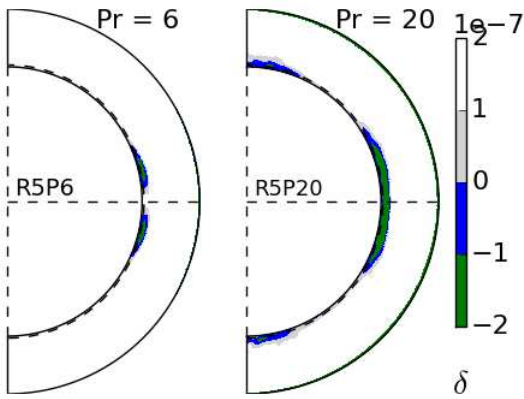


FIG. 5. Similar to Figure 2 but obtained from Runs R5P6 (left) and R5P20 (right).

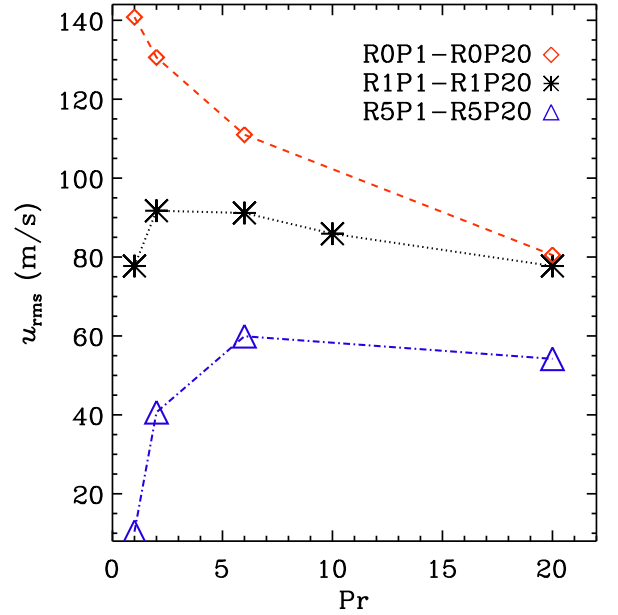


FIG. 6. Pr dependence of u_{rms} . Asterisks/black: simulations at solar rotation (R1P1–R1P20). Triangles/blue: five times solar rotation case (R5P1–R5P20). Diamonds/red: non-rotating case (R0P1–R0P20)

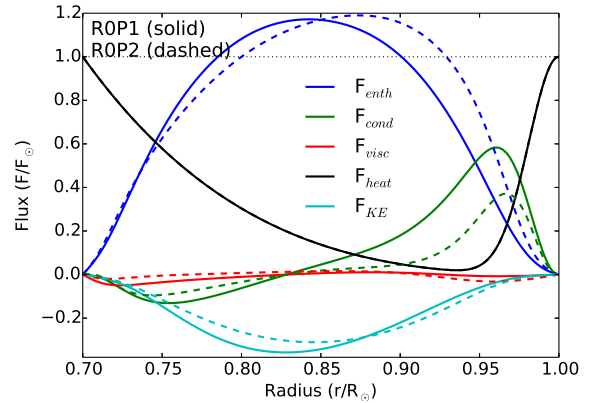


FIG. 7. Similar to Figure 4(a) but obtained from Runs R0P1 (solid lines) and R0P2 (dashed).

Convective Velocity Amplitudes

The root mean square of the convective velocity u_{rms} , averaged over the whole computation domain is shown in Figure 6. In non-rotating simulations, u_{rms} decreases with the increase of Pr, in agreement with previous findings [7, 21]. In rotating simulations, we find that u_{rms} increases first and then decreases at larger Pr but at a slower rate than the non-rotating case.

The convective velocity suppression in the non-rotating

case can be understood following the discussion presented in O'Mara *et al.* [7] (Sec. 5.2–5.4). Based on the flux balance presented in Figure 7 for Runs R0P1 and R0P2, we can write, the total flux $= L_{\odot}/4\pi r^2 \approx F_{\text{enth}} + F_{\text{cond}} + F_{\text{heat}}$. We notice that the enthalpy flux (F_{enth}) is far more dominating over other fluxes in the mid CZ. The heat flux F_{heat} which also includes the cooling near surface does not change in different runs and thus we shall omit it from the discussion here. The kinetic energy flux F_{KE} is not negligible in this set of simulations, but this does not change appreciably with the increase of Pr. This is consistent with the value of the filling factor of the downflow, f_d which does not change in this set of simulations (Table I). The contribution from the thermal conductive flux (F_{cond}) becomes increasingly negligible with the increase of Pr. This is already seen in Figure 7 that F_{cond} is negligible in Run R0P2. The disappearance of F_{cond} with the increase of Pr is really a consequence of the increasing Ra. As Ra is increased, F_{enth} dominates over F_{cond} which is well-known in solar convection simulations [1]. Therefore, in all these simulations (R0P1–R0P20) we expect, $L_{\odot}/4\pi r^2 \approx F_{\text{enth}} = v_r T$ to hold. Here T is the temperature fluctuations relative to the background which may be also regarded as the temperature deficit in the plumes relative to their surrounding. Therefore, in these runs, increasing Pr (i.e., decreasing κ), increases the temperature fluctuations (T) in plumes. Thus, to transport the same solar luminosity by the enthalpy flux, the convective velocity v_r must go down.

In computing the correlation between radial velocity and entropy fluctuations, we find that it slowly decreases with the increase of Pr; see Figure 8(a). However, the entropy fluctuation, as measured by the standard deviation of S over the horizontal surfaces, expectedly increases with the increase of Pr; see Figure 8(b). This confirms that the decrease of convective velocity is not caused by the increase of correlation between entropy fluctuation and velocity, rather it is due to the increased temperature fluctuations as discussed above.

The behavior is different in rotating simulations because rotation suppresses the convective motion as well as inhibits the downward motion of the low entropy plumes. Therefore in these runs, F_{cond} is *not* negligible. It transports a significant fraction of the total flux as seen in Figure 4(a) for Runs R1P1 and R1P2. As the rotation tends to decrease the up/down flow asymmetry by limiting the horizontal size of convection cells [27], F_{KE} is significantly reduced in rotating simulations. The filling factor is accordingly increased (meaning more symmetric up/down flows) in rotating simulations; see Table I. Hence, for Pr < 6 in the R1 set of simulations, we have, the total flux $= L_{\odot}/4\pi r^2 \sim F_{\text{enth}} + F_{\text{cond}}$. (Again we ignore F_{heat} here.). When Pr is increased from 1 to 2 i.e., from R1P1 to R1P2, F_{cond} is accordingly suppressed. This causes F_{enth} to increase, resulting in a higher con-

vective flow speed.

However, when Pr exceeds about 6 in the R1 set of simulations, the decrease of convective amplitude can be understood based on the previous discussion presented for the non-rotating case. This is because in this regime (R1P6–R1P20), F_{cond} becomes negligible and the relation $L_{\odot}/4\pi r^2 \approx F_{\text{enth}} = v_r T$ tends to hold in the mid CZ. This is already seen in Figure 4(b); also see values of L_e^p in Table I. Therefore, in all these runs, increasing Pr further decreases the convective velocity by increasing the temperature fluctuations T . The rate of velocity suppression is smaller in the R1 set of simulations in comparison to the non-rotating counterpart because, for the same Pr, F_{cond} is always higher in the rotating case. This is better reflected in the rapidly-rotation simulations (R5P1–R5P20). In Figure 9 we observe that even at Pr 6, F_{cond} is not negligible as was the case for Run R1P6 (Figure 4(b)). Thus when Pr is increased to 20 from 6 in the R5 set of simulations, the reduction of F_{cond} increases F_{enth} . This only reduces the convective velocity amplitude slightly (Figure 6).

Figure 10 shows the convective power spectra for the non-rotating (R0) and rotating (R1) sets of simulations. With the increase of Pr, convective power at smaller scales (larger horizontal wave numbers) increases. This is another indication of the increasing influence of plumes over banana cells as seen previously in Figure 3. In other words, the effective size of turbulent eddies decreases with the increase of Pr[7].

In non-rotating simulations, at larger-scales (smaller-wave numbers), the convective power decreases rapidly with the increase of Pr. In the rotating simulations, the large-scale power is relatively low for all simulations. This is very encouraging because it helps in solving the convective conundrum which says that the observed solar convection is small at large scales [4–6]. The Sun is rotating and thus if we believe that the effective Pr of the solar convection is large, then the convective conundrum might be solved. We note that this result of large-scale power suppression was also explored by Featherstone and Hindman [22], who found that the peak of the power spectrum shifts toward smaller scales with the increase of rotation rate.

In R1 set of simulations, the large-scale power shows some variation. The power increases first from R1P1 to R1P6 and then it tends to decrease again (Figure 10). Furthermore, the power increases at small scales (i.e., the increasing influence of plumes over banana cells; Figure 3) with the increase of Pr. This might change the convective Reynolds stress which is responsible for transporting the angular momentum. Therefore any change in the convective power may also lead to a change in the differential rotation pattern that is developed in these rotating convection simulations. This we explore in the next section.

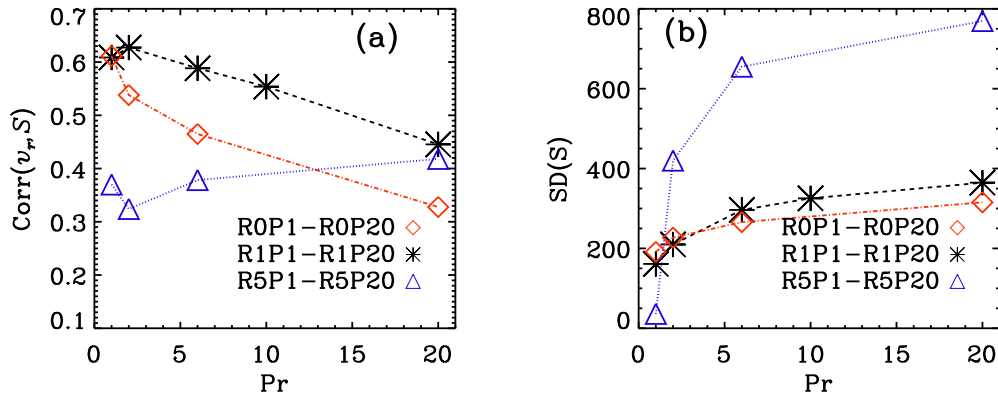


FIG. 8. Pr dependences of (a) linear Pearson's correlation coefficient between the radial velocity $v_r(r, \theta, \phi)$ and the entropy fluctuation $S(r, \theta, \phi)$, i.e., $\langle (v_r - \langle v_r \rangle_{\theta, \phi})(S - \langle S \rangle_{\theta, \phi}) \rangle_{\theta, \phi} / [\text{SD}(v_r)\text{SD}(S)]$, where $\text{SD}(x)$ is the standard deviations of x and thus $\text{SD}(S) = \sqrt{\langle [S - \langle S \rangle_{\theta, \phi}]^2 \rangle_{\theta, \phi}}$, (b) $\text{SD}(S)$ in $\text{erg g}^{-1}\text{K}^{-1}$. Both $\text{Corr}(v_r, S)$ and $\text{SD}(S)$ are obtained by taking averages of values computed at $r/R_\odot = 0.712, 0.794, 0.852, 0.909, \text{ and } 0.997$.

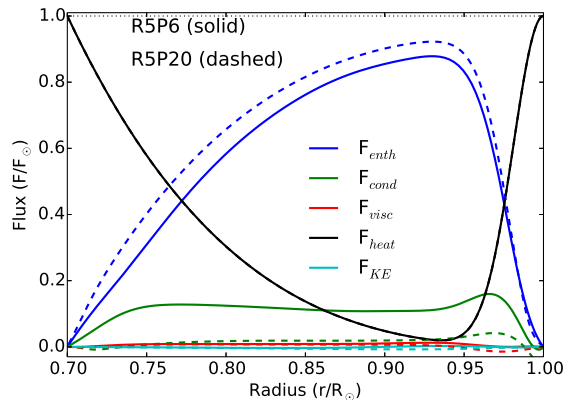


FIG. 9. Similar to Figure 4(b) but obtained from Runs R5P6 (solid lines) and R5P20 (dashed).

Differential Rotation

Figure 11 displays the temporally-averaged differential rotation $\Omega(r, \theta) = \langle u_\phi \rangle_{\phi, t} / (r \sin \theta)$. We find that for $\text{Pr} = 1$ and 2, the differential rotation is solar-like in the sense that the equatorial region rotates faster than the higher latitudes and $\Omega(r, \theta)$ increases radially outward. However, for $\text{Pr} \geq 6$ the rotation profile changes to anti-solar because $\Omega(r, \theta)$ is smaller in the low latitudes compared to higher latitudes; see values of $\Delta_\Omega^{(r)}$ and $\Delta_\Omega^{(\theta)}$ in Table I, characterizing the features of differential rotation. It is interesting to note that the Ro computed based on u_{rms} has not changed from the simulation at $\text{Pr} = 2$ to 6 (Runs R1P2 and R1P6 in Table I) but the rotation profile has flipped from solar to anti-solar. Furthermore, we notice that from $\text{Pr} = 6$ (Run R1P6) to 20 (Run R1P20), Ro decreases and thus the convection ostensibly becomes

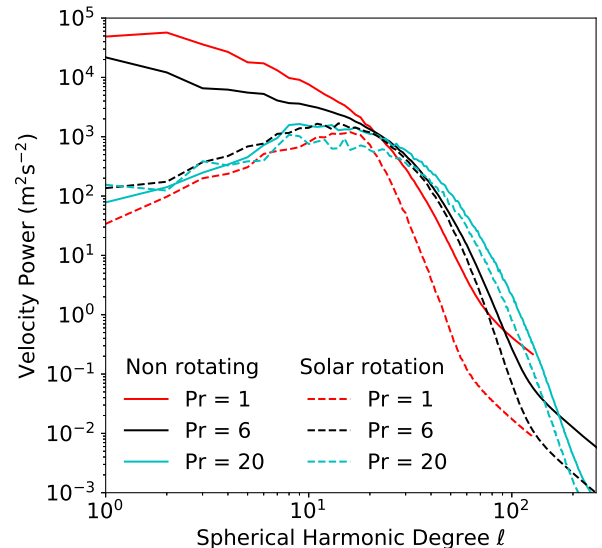


FIG. 10. Convective power spectra computed at $r = 0.74R_\odot$ from non-rotating (Runs R0P1, R0P6 and R0P20; solid lines) and rotating (Runs R1P1, R1P6 and R1P20; dashed lines) simulations. Each curve is obtained by averaging many spectra over multiple convective turnover timescales d/u_{rms} (18, 67, 18, 4, 16, and 2 for R0P1, R0P6, R0P20, R1P1, R1P6, and R1P20, respectively).

more rotationally constrained. Therefore, we expect an increasing tendency for solar-like differential rotation as in previous global convection simulations [27–29]. However, the result is opposite. The most dramatic demonstration of this is seen when comparing runs for $\text{Pr} = 1$ (R1P1) and 20 (R1P20). In these two runs, u_{rms} and Ro are the same but the rotation profiles are completely

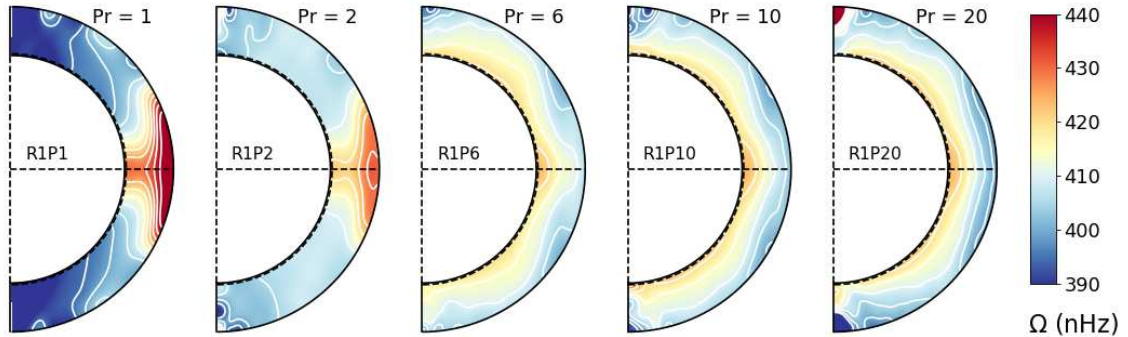


FIG. 11. Temporally-averaged rotation rate $\Omega(r, \theta)$ in nHz from Runs R1P1–R1P20 (left to right).

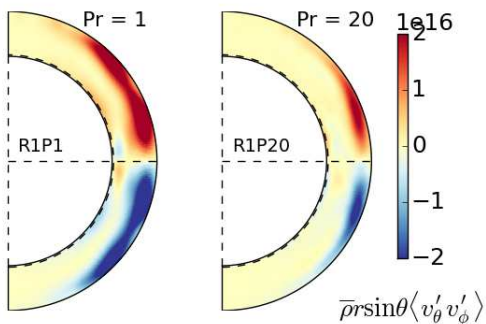


FIG. 12. The latitudinal Reynolds stress $\bar{\rho}r\langle v'_\theta v'_\phi \rangle_{\phi,t}$ (in g s^{-2}) from Runs R1P1 (left) and R1P20 (right).

opposite.

Some previous studies have shown that within a certain parameter regime, the rotating convection supports hysteresis [15, 28, 30]. That is, if the simulation is started from an anti-solar differential rotation, then it produces anti-solar differential rotation and otherwise a solar-like differential rotation is produced if started from an uniform rotation. However, this is not happening here because all simulations are started from the same initial state of uniform rotation.

The change in the differential rotation profile with the increase of Pr is caused by the inward angular momentum transport by the downward plumes. As we have discussed above, with the decrease of the heat diffusivity, the downward motion of plumes becomes stronger; see the increase of Pe with the increase of Pr in Table I. Since plumes tend to conserve angular momentum locally (in contrast to banana cells), this produces inward angular momentum transport ($\langle v'_r v'_\phi \rangle < 0$). This inward angular momentum transport in turn is responsible for establishing the anti-solar differential rotation [28, 29].

To confirm this, we compute the radial and latitudinal components of the Reynolds stress, $\bar{\rho}r \sin \theta \langle v'_r v'_\phi \rangle_{\phi,t}$, and $\bar{\rho}r \sin \theta \langle v'_\theta v'_\phi \rangle_{\phi,t}$, respectively. We find that in all simulations, the latitudinal component of Reynolds stress is positive, meaning an equatorward transport of angular momentum; Figure 12. However, the value decreases with the increase of Pr ; see $\overline{\text{RS}}_\theta$ in Table I. The radial Reynolds stress $\bar{\rho}r \sin \theta \langle v'_r v'_\phi \rangle_{\phi,t}$ shows a different behavior. Only for Runs R1P1 and R1P2, it is positive while for all other runs it is negative (Figure 13). In fact, already for Run R1P2, $\bar{\rho}r \sin \theta \langle v'_r v'_\phi \rangle_{\phi,t}$ it is negative in most of the CZ, except in low latitudes. It is the inward angular momentum transport due to plumes that makes the differential rotation anti-solar.

As mentioned above, Ro is ostensibly smaller for the simulations at higher Pr . However, these simulations exhibit more power at large wavenumbers, where the effective Ro is large (Figure 3). This excess power at small scales is another indication of the increasing importance of plumes relative to banana cells as Pr is increased.

There is a long history of studying the solar to anti-solar differential rotation transition, starting from Gilman [31] and more recently by many others [14, 15, 28–30]. These studies have shown that a transition from solar to anti-solar rotation can be achieved only by reducing the rotational effect of the convection i.e., by increasing Ro . In the past, this has been done either by decreasing the rotation rate [e.g., 32] or by increasing the convective velocity [e.g., 14, 15, 29, 30]. In our simulations, we find the solar to anti-solar transition not by increasing the global Ro , but by decreasing the thermal heat diffusivity which increases the inward angular momentum transport and decreases the equatorward angular momentum transport.

It is known that convection simulations tend to produce single-cell meridional flow when differential rotation is antisolar and multicellular otherwise [15, 29, 32]. In fact, in some studies, the antisolar differential rotation is

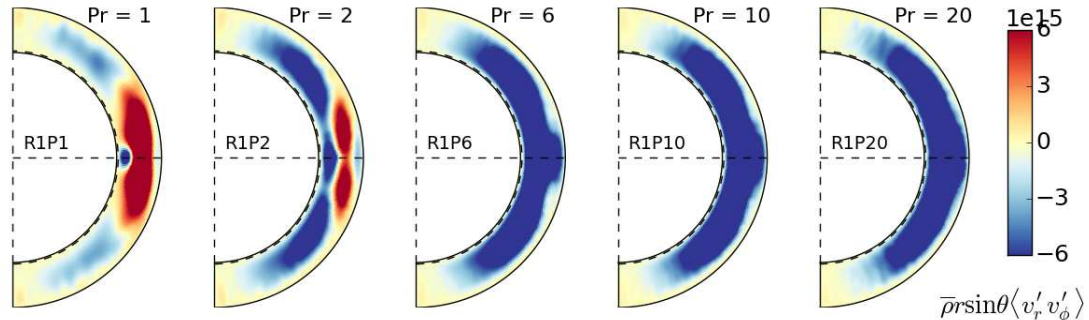


FIG. 13. The radial Reynolds stress $\bar{\rho}r\langle v'_r v'_\phi \rangle_{\phi,t}$ (in g s^{-2}) from Runs R1P1–R1P20 (left to right).

attributed to poleward angular momentum transport by the meridional flow [29, 33]. Particularly, Featherstone and Miesch [29, hereafter FM15] showed that, in the large-Ro regime, inward angular momentum transport by the convective Reynolds stress induces a single-cell meridional circulation profile (one cell per hemisphere) through gyroscopic pumping and that this induced circulation is primarily responsible for spinning up the poles relative to the equator. A similar process is also operating in our high-Pr simulations but the resulting anti-solar differential rotation profile is very different. Here inward angular-momentum transport by the increasingly plume-dominated convection induces a single-cell meridional circulation profile much as in FM15 (Figure 14, top row). However, in FM15, this induced circulation is strong enough to establish a cylindrical, Taylor-Proudman rotation profile with an Ω toward the rotation axis. In the simulations reported here, this single-cell circulation (counter-clockwise in the northern hemisphere, clockwise in the southern hemisphere) is suppressed by a strong poleward entropy gradient (Figure 14, lower right) that exerts an opposing baroclinic torque. The resulting thermal wind balance sustains an Ω gradient that is approximately radially inward (Fig. 11, right). By contrast, the entropy gradient in FM15 is equatorward and too weak to sustain significant departures from a Taylor-Proudman (cylindrical) state.

We attribute this difference to the rotational influence and the subadiabatic stratification. In FM15, as here, downward plumes are responsible for the inward angular momentum transport. However, in the simulations reported here, the transition to plume-dominated convection is achieved by an increase of the Prandtl number as opposed to an increase in the Rossby number. So, the rotational influence remains strong enough to make the convective heat flux at the poles (where plumes are not deflected by the Coriolis force) more efficient than at lower latitudes [26, 34]. This contributes to the poleward entropy gradient, particularly in the upper convection zone. In the lower convection zone, the subadiabatic

stratification established by our high-Pr simulations prevents the positive feedback between mechanical and thermal driving that can otherwise amplify the meridional circulation. This can be illustrated by first considering the opposite case of a superadiabatic convection zone. Here the circulation pattern established by gyroscopic pumping carries high-entropy fluid upward at the equator and low-entropy fluid downward at the poles. This warms the equator relative to the poles and thus acts to buoyantly enhance the circulation. In other words, gyroscopic pumping can trigger an axisymmetric convective instability that proceeds until viscous and thermal dissipation eventually halt its growth (FM15). By contrast, subadiabatic stratification suppresses this axisymmetric convection mode. Upward advection of low-entropy fluid at the equator and downward advection of high-entropy fluid at the poles establishes a poleward entropy gradient that baroclinically opposes the induced circulation and establishes thermal wind balance. In Rempel’s [35] mean-field models, this process was put forth as a promising mechanism for establishing a solar-like differential rotation profile with an equatorward (non-cylindrical) Ω gradient. Our simulations suggest that a high effective Prandtl number may support this picture by producing the requisite sub-adiabatic stratification. However, a solar-like rotation profile will only be established if the convective angular momentum flux has a sufficiently strong equatorward component in addition to an inward component.

In rapidly rotating simulations (Runs R5P1–R5P20), the convective velocity is significantly suppressed (in addition to the higher Ω) and thus the convection is more rotationally constrained (having much smaller Ro). Hence, a solar-like differential rotation is maintained in all Runs R5P1–R5P20; see Table I and top panels of Figure 15. Again, from Figure 15, we confirm that the latitudinal entropy difference is enhanced as Pr is increased, and as a result, a conical profile of differential rotation is obtained in Run R5P20.

SUMMARY AND CONCLUSIONS

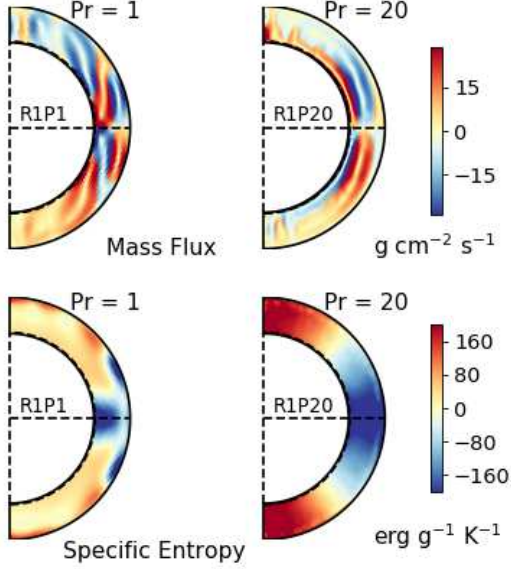


FIG. 14. Top: the mass flux ($\rho\sqrt{v_r^2 + v_\theta^2}$) of meridional flow; blue and red correspond to anti-clockwise and clockwise meridional circulation. Bottom: specific entropy $\langle S \rangle_{\phi,t}$. Left and right panels are obtained from Runs R1P1 and R1P20, respectively.

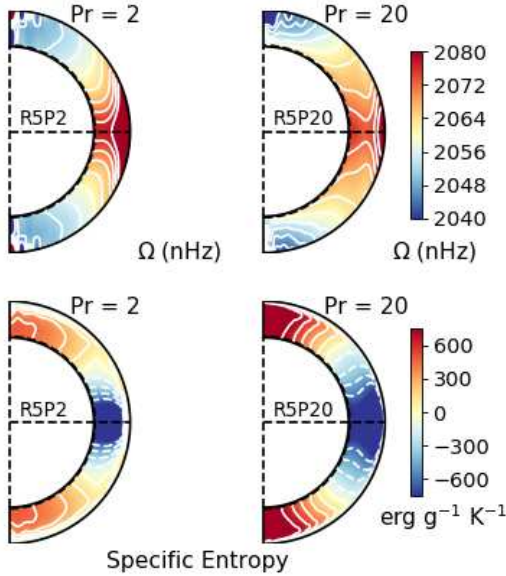


FIG. 15. Top: angular frequency Ω , bottom: specific entropy $\langle S \rangle_{\phi,t}$. Left and right panels are obtained from Runs R5P2 and R5P20, respectively.

We have considered the recently highlighted problem that solar convection simulations might be overestimating the convective power at large scales relative to observations [e.g., 4–6]. Recent studies have suggested that due to strong magnetic field produced by the small- and large-scale dynamos, the solar convection might be operating at large effective Pr and this could suppress the convective velocity amplitude [7, 13, 21]. In this paper we address this problem for the first time using global convection simulations under the influence of rotation. We explore the effect of rotation on the convective amplitude and the differential rotation and we demonstrate that what is beneficial for one may not be beneficial for the other. In particular, though a high effective Pr can reduce the amplitude of large-scale convective motions, it can also give rise to an anti-solar differential rotation.

As in previous simulations [7, 21], we consider non-magnetic (hydrodynamic) simulations with $Pr > 1$, which is intended to mimic the influence of small-scale magnetism. In our simulations, the convection is excited by introducing a heating term in the entropy equation (which mimics the radiative energy flux tabulated in the standard solar model; see O’Mara et al. [7], Featherstone and Hindman [22]) and a cooling term (which captures the efficient surface cooling near the surface; see Bekki et al. [21], Hotta et al. [23]). We conduct a series of global hydrodynamic simulations at varying κ i.e., at varying Pr and at varying rotation rate.

As reported in previous local convection simulations by Bekki et al. [21], a subadiabatic layer (with $\delta < 0$) in the lower CZ is formed in our non-rotating simulations (R0P1–R0P20) due to continuous deposition of the low entropy downward plumes. The depth of the subadiabatic layer is about 90 Mm for Runs R0P1–R0P2 and it is bigger at larger Pr. However, in simulations at the solar rotation rate, the subadiabatic layer is formed only for $Pr > 2$. The reason is that the rotation inhibits the inward transport of the cool downward plumes and thus tries to inhibit the formation of subadiabatic layer. This effect is stronger in the more rapidly-rotating simulations and therefore we observe a thin subadiabatic layer only in Runs R5P6 and R5P20.

In the non-rotating set of simulations (R0P1–R0P20), the convective velocity systematically decreases with the increase of Pr, in agreement with previous studies [7, 21]. However, in rotating sets (R1, and R5), we find a different behavior. At lower Pr, the convective velocity increases with the increase of Pr and then above a certain Pr, depending on the rotation rate, it decreases but at a slower rate than the non-rotating set. In the lower Pr range, the thermal conduction carries a significant amount of the solar luminosity and this contribution decreases with the decrease of κ (i.e., increase of Pr). This decrease of

F_{cond} with the increase of Pr, causes the enthalpy flux (F_{enth}) to increase and thus also the convective velocity.

When κ is sufficiently small, the increase of Pr does not increase F_{enth} rather it increases thermal fluctuations in the cool downflow plumes. This allows the convection to carry the solar luminosity at smaller speed. In the solar CZ, κ is very small and thus the low- κ regime is the one that is most relevant to the Sun. In this regime, the increase of Pr causes to decrease the convective flow speed.

With the increase of Pr the convective power increases at small scales and the behavior is different at large scales. In all rotating simulations, independent of the value of Pr, the convective power is smaller by about two orders of magnitude than that in non-rotating simulations at low Pr.

The most interesting result of our rotating simulations is the behavior of differential rotation with the increase of Pr. At large Pr (small κ), cool downward plumes that are formed near the surface can reach all the way to the lower CZ without losing their thermal content. This downward propagation of low entropy plumes transport angular momentum radially inward ($\langle v'_r v'_\phi \rangle < 0$), offsetting the equatorward angular momentum transport by banana cells. This inward angular momentum transport by the plumes promotes an anti-solar differential rotation.

In previous work, it had been assumed that the decrease in convective velocity amplitude with increasing Pr would help promote solar-like differential rotation by increasing the rotational influence (lower Ro). However, we find that the lower amplitude of convective motions is accompanied by a change in the convection structure that is increasingly influenced by small-scale plumes. And, such plumes tend to transport angular momentum inward, establishing a differential rotation profile in striking contrast to the solar rotation profile. Such minimally diffusive (low κ) plumes are likely also present in the solar convection zone, driven by radiative cooling in the photospheric boundary layer. So, our results cast doubt on the idea that a high effective Prandtl number may be a viable solution to the solar convection conundrum. Furthermore, our work emphasizes that any resolution of the convection conundrum that may be proposed in the future must take into account angular momentum transport as well as heat transport. This is particularly true for models that rely on small-scale convective plumes.

ACKNOWLEDGMENTS

We thank the referees for carefully reading the manuscript and providing valuable comments which help to improve the clarity of the presentation. B.B.K. was supported by the NASA Living With a Star Jack Eddy Postdoctoral Fellowship Program, administered by the University Corporation for Atmospheric Research. The code Rayleigh used in this study has been developed by Nicholas Featherstone with support by the National

Science Foundation through the Computational Infrastructure for Geodynamics (CIG). This effort was supported by NSF grants NSF-0949446 and NSF-1550901. Y.B.'s visit to HAO was supported by the Leading Graduate Course for Frontiers of Mathematical Sciences and Physics of the University of Tokyo. The National Center for Atmospheric Research is sponsored by the National Science Foundation. Computations were carried out with resources provided by NASAs High-End Computing program (Pleiades).

* bidyakarak@gmail.com

† miesch@ucar.edu

‡ bekki@eps.s.u-tokyo.ac.jp

- [1] M. S. Miesch, *Living Reviews in Solar Physics* **2**, 1 (2005).
- [2] B. B. Karak, J. Jiang, M. S. Miesch, P. Charbonneau, and A. R. Choudhuri, *Space Sci. Rev.* **186**, 561 (2014).
- [3] Å. Nordlund, R. F. Stein, and M. Asplund, *Living Reviews in Solar Physics* **6**, 2 (2009).
- [4] S. M. Hanasoge, T. L. Duvall, and K. R. Sreenivasan, *Proceedings of the National Academy of Science* **109**, 11928 (2012), [arXiv:1206.3173 \[astro-ph.SR\]](https://arxiv.org/abs/1206.3173).
- [5] J. W. Lord, R. H. Cameron, M. P. Rast, M. Rempel, and T. Roudier, *ApJ* **793**, 24 (2014), [arXiv:1407.2209 \[astro-ph.SR\]](https://arxiv.org/abs/1407.2209).
- [6] B. J. Greer, B. W. Hindman, N. A. Featherstone, and J. Toomre, *Astrophys. J Lett.* **803**, L17 (2015), [arXiv:1504.00699 \[astro-ph.SR\]](https://arxiv.org/abs/1504.00699).
- [7] B. O'Mara, M. S. Miesch, N. A. Featherstone, and K. C. Augustson, *Advances in Space Research* **58**, 1475 (2016), [arXiv:1603.06107 \[astro-ph.SR\]](https://arxiv.org/abs/1603.06107).
- [8] H. Spruit, *Memorie della Società Astronomia Italiana* **68**, 397 (1997), [astro-ph/9605020](https://arxiv.org/abs/astro-ph/9605020).
- [9] A. Brandenburg, *ApJ* **832**, 6 (2016), [arXiv:1504.03189 \[astro-ph.SR\]](https://arxiv.org/abs/1504.03189).
- [10] J.-F. Cossette and M. P. Rast, *Astrophys. J Lett.* **829**, L17 (2016), [arXiv:1606.04041 \[astro-ph.SR\]](https://arxiv.org/abs/1606.04041).
- [11] P. J. Käpylä, M. Rheinhardt, A. Brandenburg, R. Arlt, M. J. Käpylä, A. Lagg, N. Olsper, and J. Warnecke, *Astrophys. J Lett.* **845**, L23 (2017), [arXiv:1703.06845 \[astro-ph.SR\]](https://arxiv.org/abs/1703.06845).
- [12] P. J. Käpylä, M. Viviani, M. J. Käpylä, and A. Brandenburg, *ArXiv e-prints* (2018), [arXiv:1803.05898 \[astro-ph.SR\]](https://arxiv.org/abs/1803.05898).
- [13] H. Hotta, M. Rempel, and T. Yokoyama, *ApJ* **803**, 42 (2015), [arXiv:1502.03846 \[astro-ph.SR\]](https://arxiv.org/abs/1502.03846).
- [14] Y. Fan and F. Fang, *ApJ* **789**, 35 (2014), [arXiv:1405.3926 \[astro-ph.SR\]](https://arxiv.org/abs/1405.3926).
- [15] B. B. Karak, P. J. Käpylä, M. J. Käpylä, A. Brandenburg, N. Olsper, and J. Pelt, *Astrophys. J* **576**, A26 (2015), [arXiv:1407.0984 \[astro-ph.SR\]](https://arxiv.org/abs/1407.0984).
- [16] P. J. Käpylä, M. J. Käpylä, N. Olsper, J. Warnecke, and A. Brandenburg, *Astrophys. J* **599**, A4 (2017), [arXiv:1605.05885 \[astro-ph.SR\]](https://arxiv.org/abs/1605.05885).
- [17] M. Rempel, *ApJ* **789**, 132 (2014), [arXiv:1405.6814 \[astro-ph.SR\]](https://arxiv.org/abs/1405.6814).

- [18] B. B. Karak and A. Brandenburg, *ApJ* **816**, 28 (2016), [arXiv:1505.06632 \[astro-ph.SR\]](#).
- [19] P. J. Käpylä, M. J. Käpylä, and A. Brandenburg, ArXiv e-prints (2018), [arXiv:1802.09607 \[astro-ph.SR\]](#).
- [20] H. Hotta, M. Rempel, and T. Yokoyama, *Science* **351**, 1427 (2016).
- [21] Y. Bekki, H. Hotta, and T. Yokoyama, *ApJ* **851**, 74 (2017), [arXiv:1711.05960 \[astro-ph.SR\]](#).
- [22] N. A. Featherstone and B. W. Hindman, *ApJ* **818**, 32 (2016), [arXiv:1511.02396 \[astro-ph.SR\]](#).
- [23] H. Hotta, M. Rempel, and T. Yokoyama, *ApJ* **786**, 24 (2014), [arXiv:1402.5008 \[astro-ph.SR\]](#).
- [24] N. A. Featherstone and B. W. Hindman, *Astrophys. J Lett.* **830**, L15 (2016), [arXiv:1609.05153 \[astro-ph.SR\]](#).
- [25] N. H. Brummell, T. L. Clune, and J. Toomre, *ApJ* **570**, 825 (2002).
- [26] M. S. Miesch, J. R. Elliott, J. Toomre, T. L. Clune, G. A. Glatzmaier, and P. A. Gilman, *ApJ* **532**, 593 (2000).
- [27] B. P. Brown, M. K. Browning, A. S. Brun, M. S. Miesch, and J. Toomre, *ApJ* **689**, 1354-1372 (2008), [arXiv:0808.1716](#).
- [28] T. Gastine, R. K. Yadav, J. Morin, A. Reiners, and J. Wicht, *MNRAS* **438**, L76 (2014), [arXiv:1311.3047 \[astro-ph.SR\]](#).
- [29] N. A. Featherstone and M. S. Miesch, *ApJ* **804**, 67 (2015), [arXiv:1501.06501 \[astro-ph.SR\]](#).
- [30] P. J. Käpylä, M. J. Käpylä, and A. Brandenburg, *Astrophys. J* **570**, A43 (2014), [arXiv:1401.2981 \[astro-ph.SR\]](#).
- [31] P. A. Gilman, *Geophysical and Astrophysical Fluid Dynamics* **8**, 93 (1978).
- [32] G. Guerrero, P. K. Smolarkiewicz, A. G. Kosovichev, and N. N. Mansour, *ApJ* **779**, 176 (2013), [arXiv:1310.8178 \[astro-ph.SR\]](#).
- [33] W. Dobler, M. Stix, and A. Brandenburg, *ApJ* **638**, 336 (2006), [astro-ph/0410645](#).
- [34] L. L. Kitchatinov and G. Ruediger, *Astrophys. J* **299**, 446 (1995).
- [35] M. Rempel, *ApJ* **622**, 1320 (2005), [astro-ph/0604451](#).